Electronic Supplementary Information (ESI)

Magnetic field and ultrasound induced simultaneous wireless energy harvesting

Sumanta Kumar Karan,*[a] Sujay Hosur,[b] Zeinab Kashani,[b] Haoyang Leng,[a] Anitha Vijay,[c] Rammohan Sriramdas,[a,d] Kai Wang,[a] Bed Poudel,[a] Andrew D. Patterson,[c] Mehdi Kiani,*[b] and Shashank Priya*[a]

[a]Department of Materials Science and Engineering, Pennsylvania State University, University Park, PA 16802, USA

[b]School of Electrical Engineering and Computer Science, Pennsylvania State University, University Park, PA 16802, USA

[c]Department of Veterinary and Biomedical Sciences, The Pennsylvania State University, University Park, Pennsylvania 16802, USA, The Pennsylvania State University, University Park, PA 16802, USA

[d]Department of Mechanical Engineering, Amrita School of Engineering, Coimbatore, Amrita Vishwa Vidyapeetham 641112, India

*Correspondence to: skk5867@psu.edu and sumanta.karan.fula@gmail.com; muk42@psu.edu; sup103@psu.edu

Note S1. Fabrication of piezoelectric disk

2 mol.% MnO_2 and 0.125 wt.% CuO co-doped PIN-PMN-PT matrix powders were synthesized using two-step columbite precursor method.[1, 2] The raw materials of In_2O_3 (99.9%) and Nb_2O_5 (99.9%) were used to prepare $InNbO_4$ precursor at 1100 °C for 7 h. Next, the stoichiometric amounts of PbO (99.9%), $InNbO_4$, $MgNb_2O_6$ (99.9%), TiO_2 (99.8%), and MnO_2 (99.9%) were wet mixed in ethanol by ball milling for 24 h. The dried mixtures were calcined at 850 °C for 4 h to obtain the pure perovskite phase. The calcined powders were ball milled again with 1.5 wt% excess PbO and 0.125 wt% CuO in ethanol for 48 h to decrease the particle sizes. After second ball milling, the dried powders were pressed to form 0.5-inch diameter discs. The discs were then cold isostatically pressed at 200 MPa for 1 min. Lastly, the discs were sintered at 1200 ^{o}C for 6 h in air. The crystal phases and microstructures of the sintered discs were characterized by using X-ray diffraction (XRD, PANalytical Empyrean) and field-emission scanning electron microscopy (FE-SEM Apreo), respectively (Fig. S1a,b).

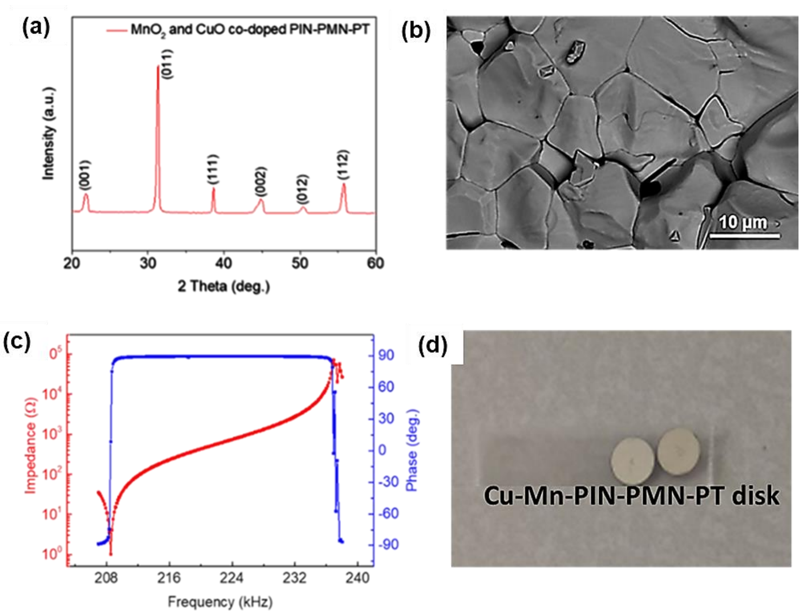

Fig. S1. (a) XRD pattern and (b) SEM image of 2 mol.% MnO_2 and 0.125 wt% CuO co-doped PIN-PMN-PT ceramics. (c) Impedance and phase angle spectra of 2 mol.% MnO_2 and 0.125 wt% CuO co-doped PIN-PMN-PT ceramics. (d) The picture of piezoelectric materials used in the present study.

To conduct the electrical measurements, the silver paste was coated on both sides of the sintered discs and then fired at 550 ^{o}C for 30 min. The discs were then poled at 30 kV/cm for 30 min at 140

^{o}C. The piezoelectric constant d_{33} was measured by a quasi-static d_{33} meter (YE2730A, APC Products). The dielectric permittivity ε_r and dielectric loss *tan* δ were measured using a multifrequency LCR meter (HP4284A) at 1 kHz. The electromechanical coupling coefficient k and mechanical quality factor Q_m were calculated by resonance and antiresonance technique (Fig. S1C) using an impedance analyzer (Keysight E4990A).

Relaxor-PT ferroelectrics such as $Pb(In_{1/2}Nb_{1/2})O_3$-$Pb(Mg_{1/3}Nb_{2/3})O_3$-$PbTiO_3$ (PIN-PMN-PT) can show higher piezoelectric properties compared to commercial PZT.[3, 4] The MnO_2 and CuO co-doped PIN-PMN-PT piezoceramics exhibited a high piezoelectric coefficient (d_{33} ~ 370 pC N^{-1}), high mechanical quality factor (Q_m ~ 2200), and low dielectric loss (*tan* d ~ 0.6%). The transducer using this material was fabricated through a modified dicing-and-filling technique as discussed in Fig. S1 to optimize the device performance. As presented in the X-ray diffraction (XRD) pattern and a scanning electron microscopy (SEM) image (ESI, Fig. S1), the synthesized MnO_2 and CuO co-doped PIN-PMN-PT ceramics exhibited a perovskite structure without noticeable secondary phases and dense grain microstructures. The as-fabricated piezo-elements exhibit a resonant frequency of 208 kHz (Fig. S1C) along with high electromechanical coupling coefficient k_p and voltage coefficient g_{33} (*e.g.*, $k_p \approx$ 0.54, $g_{33} \approx$ 27.7×10^{-3} V.m/N ×10^{-3}), ensuring the acoustic sensitivity and high output capabilities of the device. Some important acoustic and electrical parameters of the as-fabricated Cu-Mn-PIN-PMN-PT ceramic are summarized in Table S1.

Table S1. Summary of the properties of synthesized piezoelectric materials.

Piezoelectric material	Permittivity of piezo material ε_{33}^T/ permittivity of free space (ε_o)	*Dielectric loss (tan* δ) (%)	*Piezoelectric charge constant (*d_{33}) (pC/N)	*Piezoelectric voltage constant (*g_{33}) (×10^{-3} Vm/N)	*Electromechanical coupling factor (*k_P)	*Mechanical quality factor (*Q_m)
Cu-Mn-PIN-PMN-PT	1507	0.6	370	27.7	0.54	2200

Note S2. Fabrication of MUDG device

To fabricate MUGD devices, we have used high power piezo ceramic (Cu-Mn-PMN-PT) as piezoelectric layer and Metglas alloy as magnetostrictive layer. Prior to fabrication, the Metglas was machined into disk shape using a Hole-Punch machine. The manufactured piezoelectric disks had the diameters of 9.8mm with different thickness of 0.8mm and 0.5mm. Two different thickness of piezoelectric materials was used to fabricate the devices with different number of magnetostrictive layers (22µm).

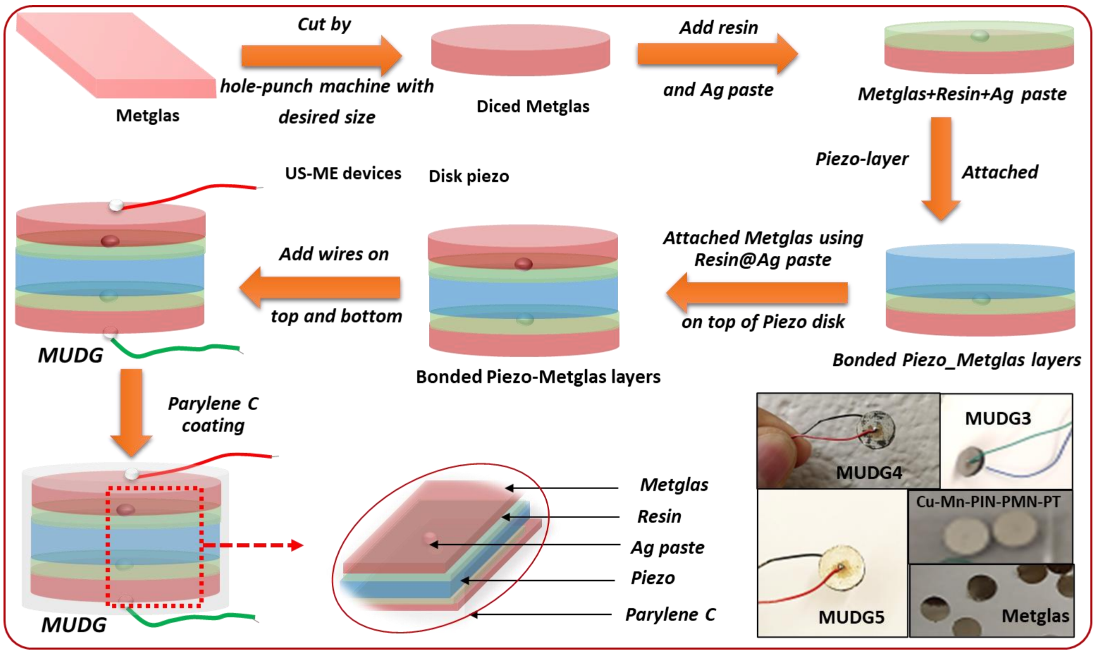

Fig. S2: Procedural details for MUDG device fabrication shown schematically and real images of the devices.

The MUGD device was in the form of a sandwich, with the piezoelectric material sandwiched between the magnetostrictive layers (Metglas). The layers were attached using thin epoxy adhesive (DP-460, 3M) and electrically connected using silver paste (Leitsilber 200 Silver Paint, Ted Pella) across the layers to ensure the electrical connection in the composite structure. Afterward, we placed the devices under weight of ≤15kg overnight at room temperature to cure the epoxy and finalize the devices. The excess overspill was removed by hand polishing the sides with 1200/P4000 grit sandpaper, Finally, copper wires were soldered on top and bottom side of the MUDG devices to act as electrodes during measurements. Following basic testing of the transducer (impedance and magnetic power measurements in air), it was subsequently coated with ~10 µm of biocompatible Parylene-C using the vapor deposition method. We have fabricated the MUDG device by laminating piezoelectric and magnetostrictive layers (Fig. S2). The layered type composites have attracted attention due to high values of ME coupling coefficient.[5, 6] It is noteworthy, in layered structures, a higher strain is generated in response to the applied magnetic field as the piezoelectric layer is able to maintain its properties in the end composite as compared to 0-3/1-3 structured composites.[5, 7] To optimize the performance of the device, different number of Metglas layers were attached on top (3,4,5 and 6) and bottom (3,4,5 and 6) of the piezoelectric layer using the above-mentioned process and these samples were termed as MUDG3, MUDG4, MUDG5 and MUDG6. For each set, we made three devices for measurement of the output performance. The detailed process for the fabrication is discussed below in Fig. S1 The devices are designed to be ~10 mm in diameter and have thickness ranging from ~0.95 mm to ~1.1 mm.

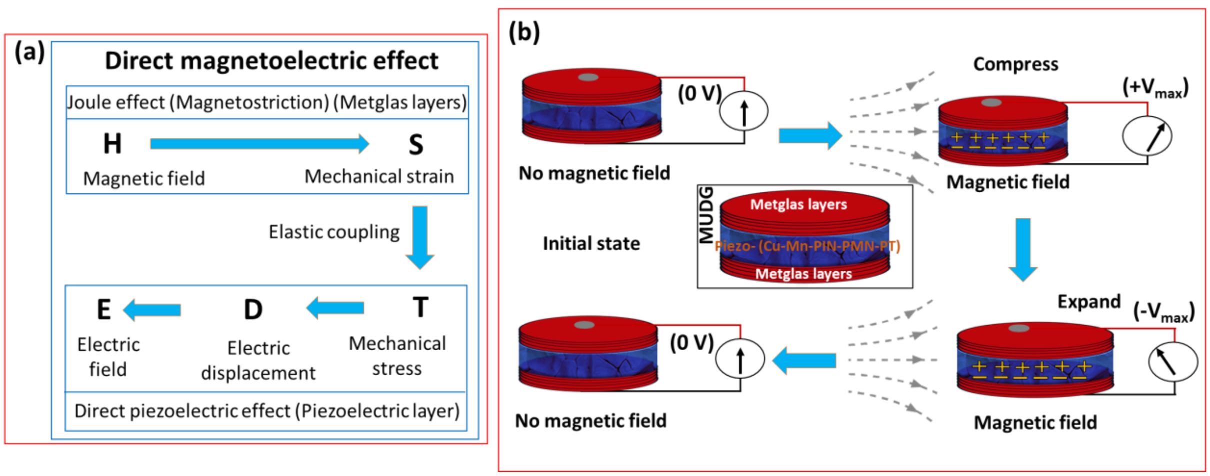

Fig S3. (a) The transformation of a magnetic field (H) into an electric field (E) occurs through the direct magnetoelectric (ME) effect, facilitated by the Joule effect in the magnetostrictive layer and the direct piezoelectric effect in the piezoelectric layer, within an ME transducer. (b) The working mechanism of electricity generation from MUDG device via magnetoelectric effect under applied magnetic field.

The direct magnetoelectric phenomena within laminate composites, composed of a piezoelectric layer (Cu-Mn-PIN-PMN-PT is used here) and magnetostrictive layers (Metglas is used here), can be illustrated using the Figure S3a. In this structure, H represents the magnetic field, S stands for mechanical strain, T denotes mechanical stress, D signifies electric displacement, E represents the electric field, and M denotes magnetization. The direct magnetoelectric effect operates as follows: The input magnetic field H induces a strain S in the magnetostrictive layer through magnetostriction. This strain is then transmitted to the piezoelectric layer via elastic coupling.

Subsequently, a mechanical stress T emerges in the piezoelectric layer due to elastic stiffness, leading to the creation of surface charge density (D) or polarization through the direct piezoelectric effect (Fig. S3a,b). The deformation results in the separation of positive and negative charges, giving rise to an electric dipole and creation of a piezo-potential. When an external circuit is added to the deformed piezoelectric material, it facilitates a current flow through the external electrodes, yielding a positive signal. Conversely, during decompression or expansion, the current can reverse its direction in the external circuit, counteracting the piezoelectric potential and producing a negative signal.

Note S3. Optimization of DC magnetic field response from generated strain and piezomagnetic (PM) coefficient

The magnetic energy harvesting performance of the MUDG devices was investigated using a customized Helmholtz coils that generates an AC magnetic field (H_{AC}) and electromagnets responsible for applying DC magnetic field. To confirm the optimum DC magnetic field, we have repeatedly measured the strain value of different MUDG devices using strain sensor by changing DC magnetic field as shown Fig. S4.

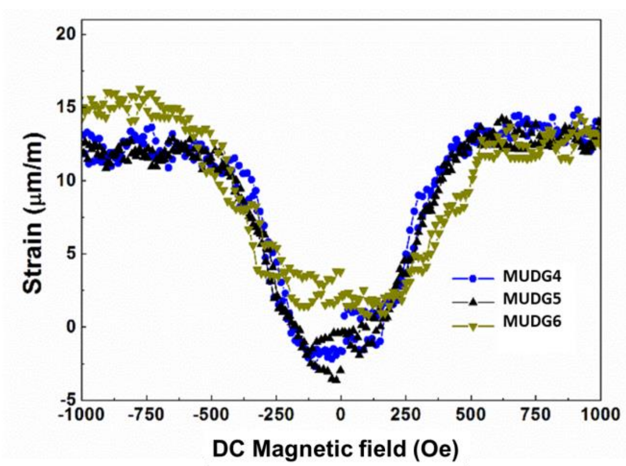

Fig. S4. The strain vs. DC magnetic field strength for different MUDG devices with different number of magnetostrictive layers. It is noteworthy that the magnetic field strength Oe can be represented as A/m unit i.e. 1 Oe = 79.58 A/m.

Fig. S4 shows that the strain values increased with increasing of DC magnetic field and saturated at higher DC magnetic field. The maximum strain value of 16.27 has been achieved for MUDG6 device because of the larger number of magnetostrictive layers. But maximum stain was not responsible for optimum DC magnetic field. To know the optimum DC magnetic bias, the piezomagnetic (PM) constant (Fig. S5) has been considered and calculated from DC field vs. strain curve as described in Fig. S4.

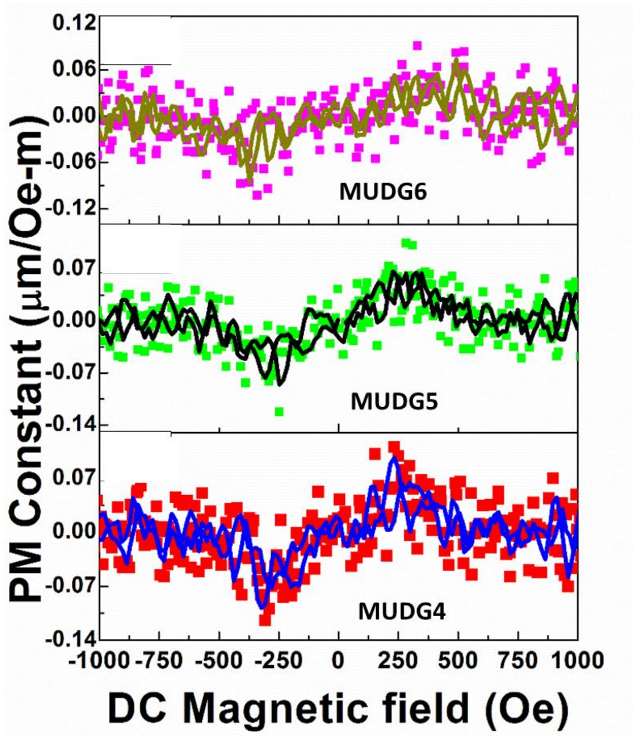

Fig. S5. The variation of piezomagnetic constant with DC magnetic field strength.

The PM constant value of 0.122 was obtained for MUDG5 device which is the highest among all the devices. The highest PM constant for every MUDG device predicts the optimum DC magnetic field corresponding to strain values as shown in Fig. S5 and Table S2. The optimal DC magnetic bias for MUDGs measured from strain vs. DC magnetic curve at highest PM constant are comparable to the optimal DC magnetic field measured from magnetic moment vs. DC magnetic bias plot in VSM measurement (Fig. S6). High piezomagnetic constant signify high output performances which clearly reflects the performance of MUDG5 device under constant AC magnetic field (100 μT), and optimum DC magnetic field at constant working frequency.

Table S2. The strain, piezomagnetic constant and optimum DC magnetic field strength of different MUDG devices with different number of magnetostrictive layers.

Metglas layers and Devices	Max strain	Strain at optimum DC	Optimum DC bias in magnetoelectric measurement	PM constant and optimum DC bias in stain measurement
4 Layers (MUDG5)	14.20	4.47	240 Oe (19.1 kA/m)	0.110 and 233 Oe (18.54 kA/m)
5 Layers (MUDG5)	14.22	6.19	285 Oe (22.68 kA/m)	0.122 and 282 Oe (22.4 kA/m)
6 Layers (MUDG6)	16.27	8.11	355 Oe (28.25 kA/m)	0.101 and 340 Oe (27.05 kA/m)

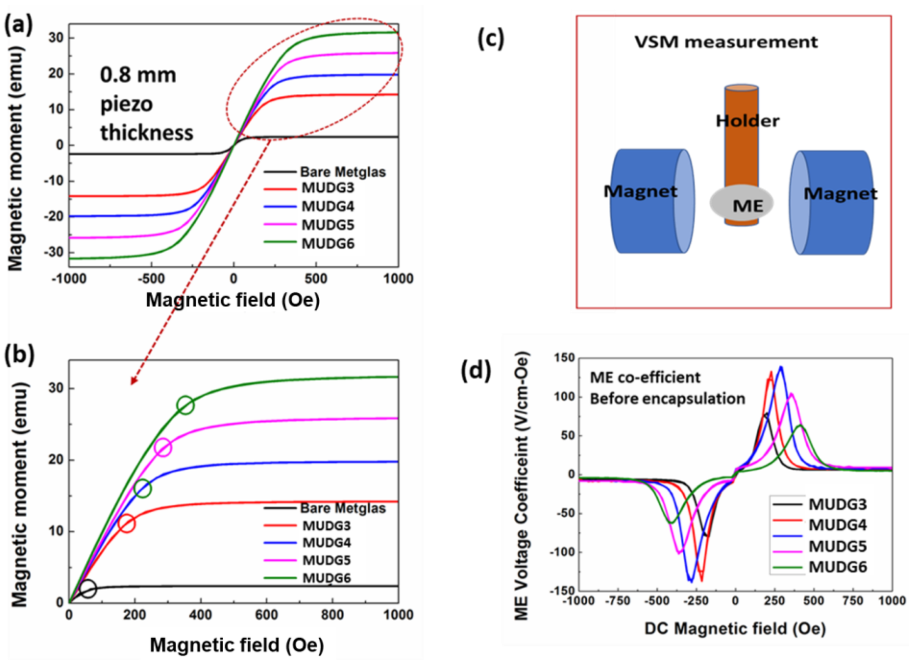

Fig. S6. (a, b) The variation of magnetic moment with DC magnetic field for different MUDG devices and (c) the magnetic moment measurement set up for different MUDG devices using VSM. (d) The ME voltage coefficient vs. DC magnetic behaviour of different MUDG devices before encapsulation in air environment.

Note S4. The impedance behaviour of the MUDG devices

The working frequency and impedance profile of the MUDG devices has been characterized in air and water from impedance analyser (E5071C, Tektronix, USA) as shown in Fig. S7. The piezoelectric disks used for the fabrication of the MUDG devices is not exactly same but very similar in the dimension. With the increase of the magnetostrictive layers, the impedance decreases which clearly indicates the effect of layers and power level. The working frequency (antiresonance frequency) of the MUDG device increases with the increasing magnetostrictive layers but for MUDG5 device the frequency is less than the MUDG4 device. The radius of the piezoelectric disk used for the fabrication for MUDG5 device is slightly more than the piezoelectric disk used for the fabrication of MUDG4 device. Also, the dimension of the magnetostrictive layers for MUDG4 device is slightly more compared to the MUDG5 device. However, the power level of the MUDG devices in the present study is clearly related to effect of number of magnetostrictive layers and its optimization.

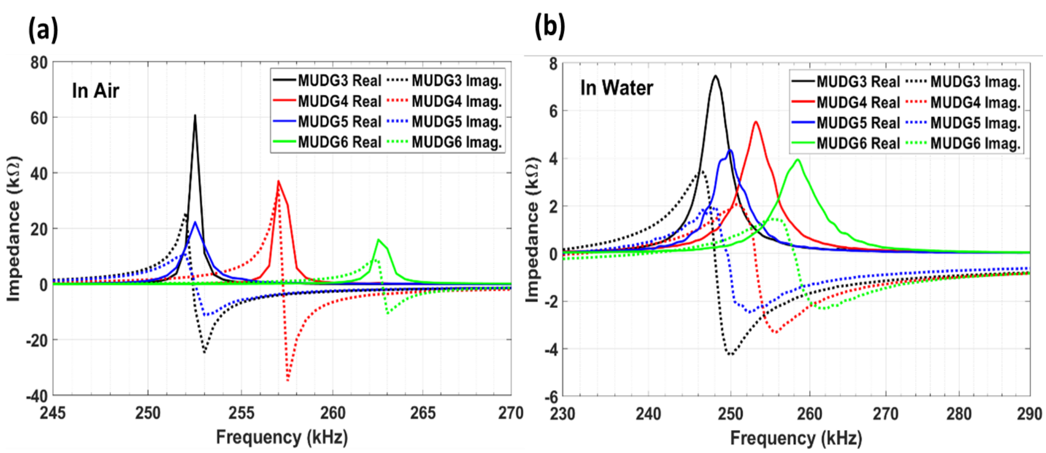

Fig. S7. The measured impedance (real and imaginary) for the MUDG devices in (a) air and (b) water medium.

The impedance and frequency profiles of the MUDG device under water shows the similar tendency. The impedance of the devices decreases due to the water medium which is a general trend. Under water, the resonance frequency also decreases for the MUDG devices compared with frequency measured in air medium.

Note S5. Quality factor and relation between DC magnetic field with frequency/external load

The quality factor (Q) can be obtained from voltage vs. frequency curve, as the ratio of measured maximum voltage (at the working frequency) to the half power bandwidth, as shown in Fig. S8a for MUDG5 device.[8] The Q-factor with an increasing DC magnetic field is as shown Fig. S8b. Fig. S8c shows the dependence of the optimum DC bias values for the different MUDG devices. Q increasing with the DC magnetic bias indicates that the fabricated devices are in good condition. Fig. S8d signifies the working frequency may also change with the changing of DC bias applied during energy harvesting measurement.

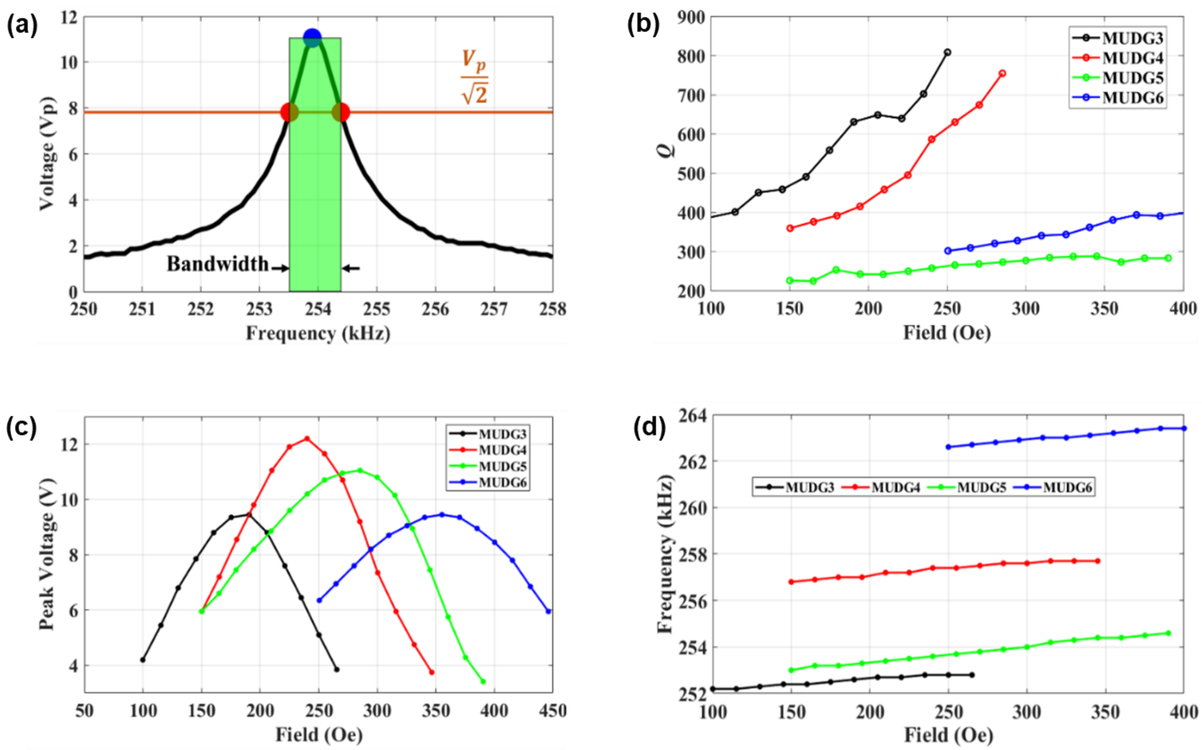

Fig. S8. (a) Half power bandwidth method for experimental estimation of Q. (b) Trend of Quality factor (Q) with DC magnetic field. (c) Peak voltage variation with DC magnetic field. (d) Variation of frequency with DC magnetic field corresponding to the peak voltage in Fig. S8c.

Table S3. The dimension of the MUDG devices and the properties in air medium

Device	Thickness and diameter (mm)	Capacitance (nF)	Working frequency (kHz)	Optimum DC field after encapsulation (Oe) (1 Oe=79.58 A/m)	Power before encapsulation (μW) at 100 μT AC magnetic field (air medium)	Power after encapsulation (μW) at 100 μT AC magnetic field (air medium)	Q after encapsulation (air medium)
MUDG3	1.02 and 10.20	1.16	252.6	190±20	148	147	350
MUDG4	1.06 and 10.31	1.08	257.6	230±20	375	373	465
MUDG5	1.07 and 10.20	1.22	254.0	300±20	660	650	290
MUDG6	1.16 and 10.28	1.16	263.3	360±20	300	293	309

Note S6: COMSOL simulation for magnetoelectric and ultrasound effect

The cylindrical model was built using the COMSOL multiphysics with the constituent Metglas magnetostrictive phase and PZT-4 piezoelectric layers—the diameter of the piezo discs and metglas layers was kept at 9.9 mm. The piezoelectric layer with a thickness of 0.8 mm and the metglas layer with a thickness of 0.115 mm (equivalent to 5 layers) were used for the simulation. The model was first constructed in 3D and then reduced to 2D-axisymmetric using the geometric reduction feature to reduce the computation time. The ME composite was placed in the airspace of 100 mm diameter. Regarding material properties, inbuilt PZT-4 data was used for the piezoelectric layer and Metglas properties provided by the manufacturer were used.

Note S7. Thickness ratio of MUDG device, Parylene-C coating and output measurement in different planes

The thickness ratio is an important factor to indicate the power of the MUDG devices and it is 0.15 for MUDG5 (Fig. S9a). The thickness ratio (t_m/t_p) is defined as the ratio of thickness of magnetic layer (t_m) with thickness of the piezoelectric material (t_p). The leakage and safety issue of the devices under water/tissue is managed by using the Parylene-C coating over the device. The reason behind using Parylene-C coating (6-8 µm) is related to its corrosion and chemical resistance with biocompatibility. This protects the devices from the water and probable toxic effect of chemicals. The performance of the Parylene-C coated (6-8µm) MUDG5 gives similar output power (0.65 mW) as compared to devices without Parylene-C coating (0.66 mW) as shown in Fig. S9b. But PDMS encapsulated MUDG5 gives lower output power (0.42 mW) compared to Parylene-C coated MUDG5 device (Fig. S9b). The decrease in performance can be attributed to the difference in thickness between the PDMS coating, which is around 500µm, and the Parylene-C coating which is only 6-8µm thick. Maintaining the exact thickness of PDMS on the device is challenging, as it is difficult to control the edges of the device during the hand or spin coating process. Conversely, Parylene-C coating allows for more precise thickness control. Additionally, if the device is coated with a thinner layer of PDMS (6-8µm), there is a higher likelihood of damaging the coat near the shouldering area of the electrical wire. [9] Therefore, Parylene-C coating is a better option for controlling thickness and achieving optimal device performance, even though PDMS is more transcutaneous in nature. [9, 10]

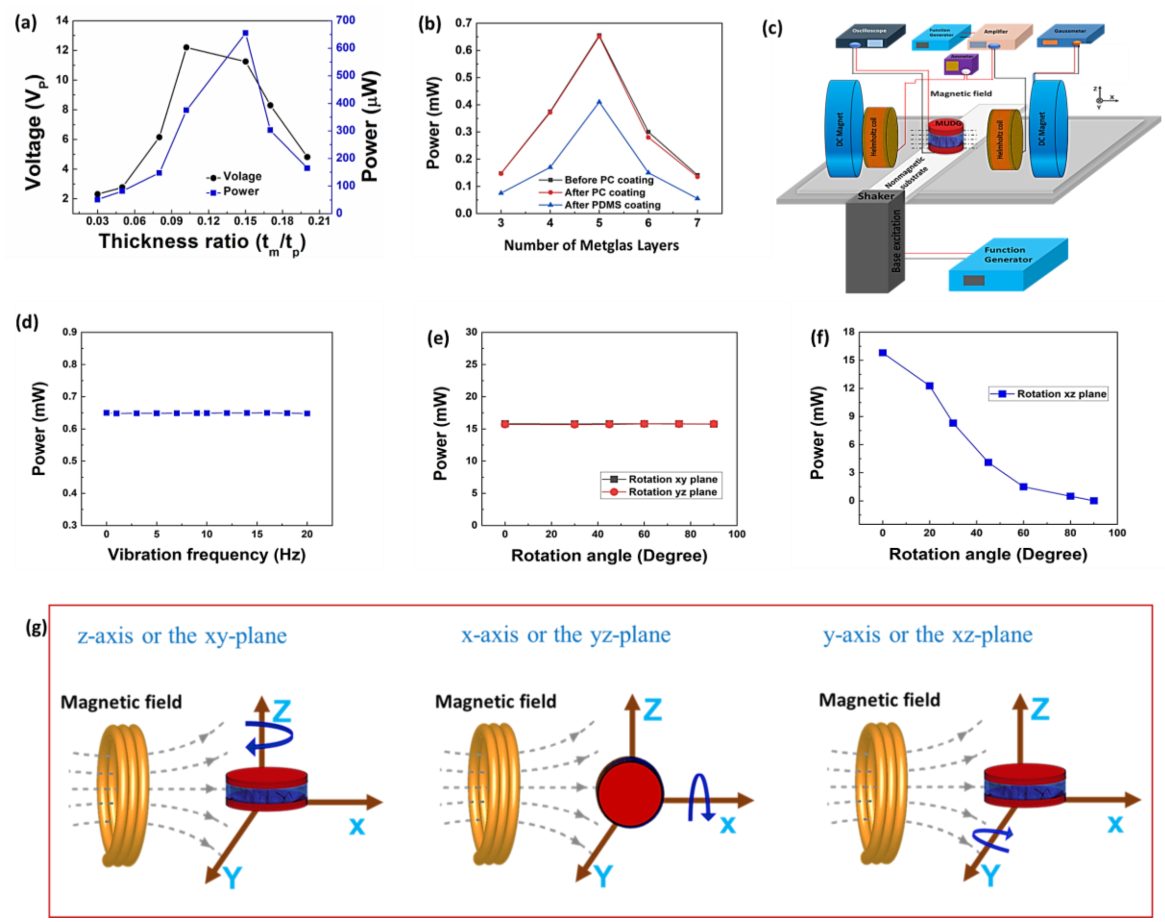

Fig S9. (a) The generated voltage and power behaviour with thickness ratio of MUDGs. (b) The comparison of output power with number of magnetostrictive layers. (c) Measurement set-up to check the effect of additional vibration applied to the MUDG device during magnetoelectric output power measurement. (d) The dependence of output power from MUDG device under 100 T AC magnetic field and external mechanical vibration with 1-20 Hz frequency. (e) The impact of output power under AC magnetic field (500 µT) when rotating the MUDG5 device along the z/x-axis (in xy/yz plane). (f) The power output from MUDG5 device under AC magnetic field (500 µT) when rotating the device along the y-axis (in xz plane). (g) The angular misalignment in different 3 axes – the z-axis or the xy-plane; the x-axis or the yz plane and the y-axis or the xz-plane.

To understand the effect of mechanical vibration in the 1-20 Hz frequency range (that mimics human body motion) on the performance of MUDG, the output power of MUDG device was measured at working frequency (250±5 kHz) in air under 100µT magnetic field and under additional vibration applied using cantilever through shaker (Fig. S9c) with frequency ranging from 1 to 20 Hz at an acceleration of 1g. The results shows that there is no significant change

(~0.2-0.3%) in the power of the MUDG device (Fig. S9d). The generated power from MUDG device without adding any vibration is found to be 0.650 mW (at 100 μT), whereas the power from MUDG device under vibration (5Hz) is 0.648 mW (at 100 μT). Moreover, the working frequency of MUDG device is the range of ~250±5 kHz which is far from the body movement vibration frequency range of 1-20 Hz with acceleration in the range 0.6-1.22g.[11, 12] Hence, there is minimal effect on output performance of MUDG device. Hence, in a real-world application, the body movement, does not affect the MUDG device's performance.

Note S8. Magnetoelectric measurement set up under water

To evaluate the output performance of the MUDG devices under magnetic field and ultrasound, we immersed the devices in water as illustrated in Fig. S10a. Water was chosen as the medium for our research because it is suitable for both magnetic and ultrasound energy, and it has a similar acoustic impedance as that of tissue. To harvest magnetic energy under water, we developed a system (Fig. S10a) with a small water tank that fits between Helmholtz coils and DC electromagnets. The MUDG devices were coated with Parylene-C to protect them and placed in the water tank with the bottom part of the device flat against the tank. To allow the wires to exit the water tank, we created two small holes in the container, which we sealed with hot glue to prevent water leakage. We then checked for any leaks using water, as shown in Fig. S10b.

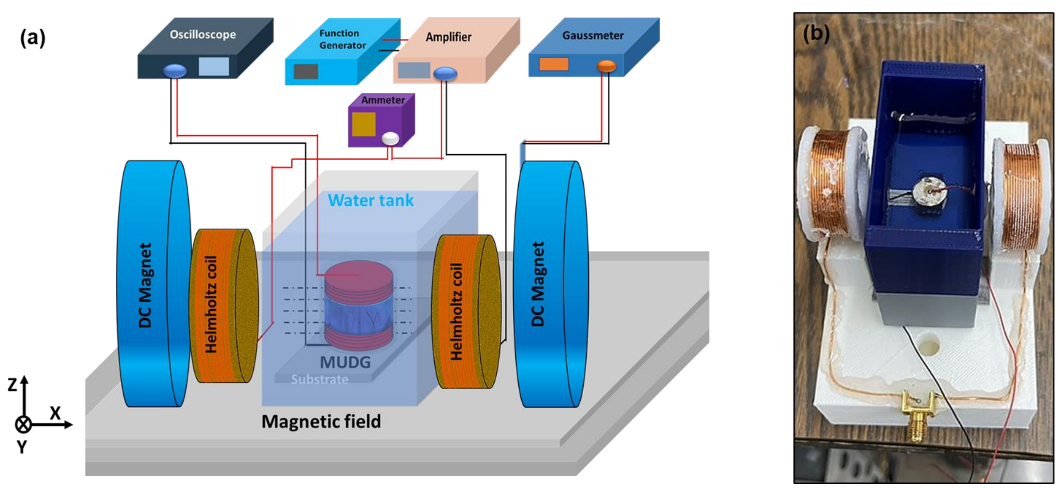

Fig. S10. (a) The magnetoelectric measurement set up under water environment. (b) The 3D printed small water tank was used for magnetoelectric and ultrasound measurement in water medium.

The output voltage performances of the MUDG5 devices relates linearly under high AC magnetic field strength at constant DC bias and at constant frequency (Fig. S11a). As the AC magnetic field strength increases, the output voltage (Vp) of the MUDG5 device also increases and exhibits nearly linear behaviour.

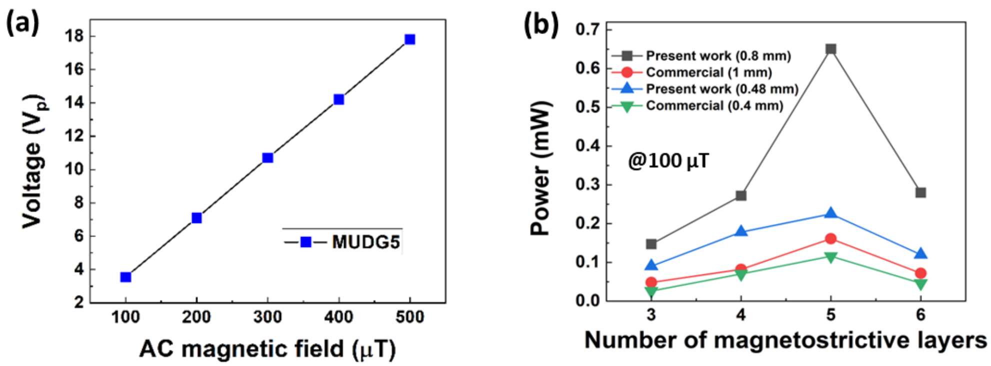

Fig. S11. The variation of AC magnetic field strength (at constant DC bias) with the generated output voltage from MUDG5 device and constant frequency (250kHz).

Different piezoelectric disk thickness (0.5 and 0.8 mm thick) was used and compared with the commercial piezoelectric disk (0.4 and 0.8 thick) with same number of magnetostrictive layers (Fig. S11b).The MUDG5 device shows ~4 times output power compared with the 1 mm thick commercial piezo disk based device, whereas 0.48 mm thick piezo disk based MUDG5 device shows ~2 times better performance compared with the 0.4 mm thick commercial piezo disk-based device .

Note S9. Ultrasound measurement set up

Custom designed 3D printed holder was used to adjust the angle alignment of the MUDG devices with the commercial transducer (Fig. S12a,b). During the measurement, both the transducer and the MUDG devices were immersed in water to realize the matching of the acoustic impedance which is similar to that of the tissue because the air has very high acoustic impedance which can drastically reduce power transfer efficiency.[13] To find the impedance profile of commercial ultrasound transducer used as a transmitter in our measurements, the S-parameter measurements were conducted using a network analyzer. The impedance profile of transducer and input power at different driving voltage in the frequency range of 225 – 265 kHz is presented in S12c,d.

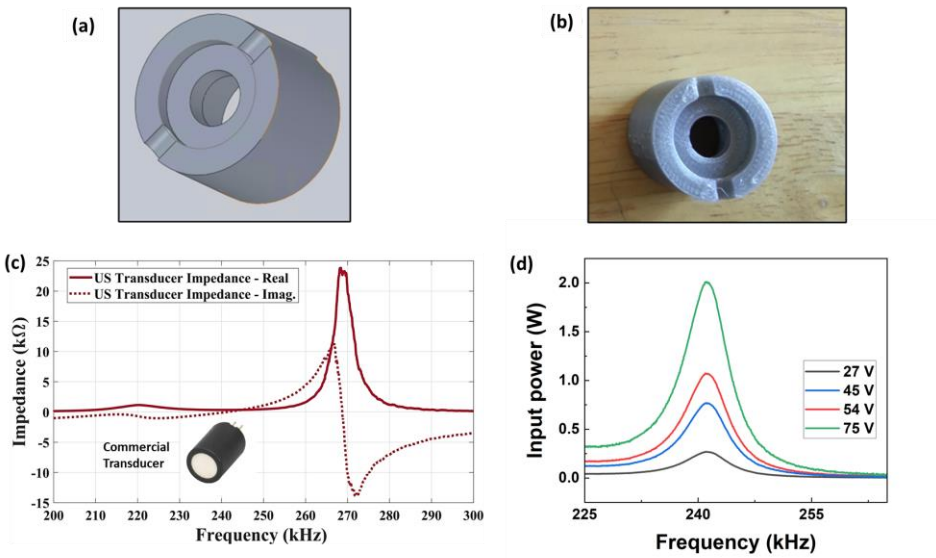

Fig. S12. (a, b) 3D model and real image of holder to hold the MUDG devices to avoid any alignment problem for output measurement under tissue. (c) The impedance profile of the commercial transducer and (d) the behaviour of resonance frequency with input power applied to the transducer.

Note S10. Relationship between input and output voltage for ultrasound energy harvesting and working principle

The applied input voltage has a linear relationship with output voltage of MUDG devices at constant working frequency, facilitating tunable property of the device (Fig. S13a,b).

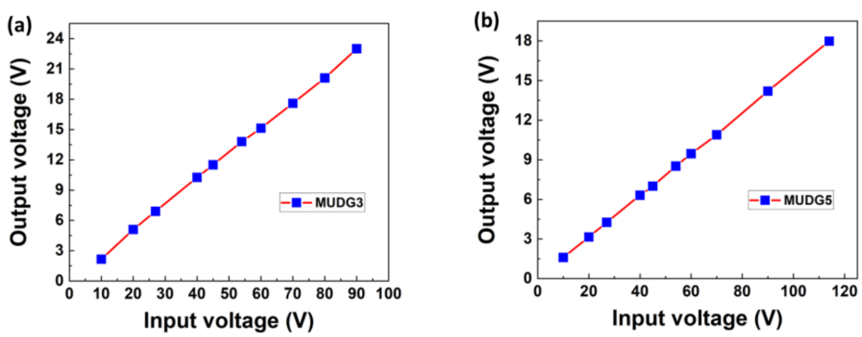

Fig. S13. The relation between the applied input voltage (Vp-p) and received output voltage (Vp-p) of MUDG3 at 237kHz and MUDG5 at 250kHz, respectively.

The principle of generation of electricity in piezoelectric material under ultrasound pressure can be explained by invoking direct piezoelectric effect as shown in Fig. S14a. The mechanical stress

(T) can deform the piezoelectric layer, leading to the creation of surface charge density (D) or polarization through the direct piezoelectric effect. This charge separation results in the generation of an output voltage or electric field within the piezoelectric layer. Under external ultrasound pressure (dynamic pressure) on MUDG device, it causes deformation of the piezoelectric layer present in the ME device. This deformation leads to the separation of positive and negative charges, creating an electric dipole and generating a piezopotential. When an external circuit is connected to the continuously deforming piezoelectric material, it results in a flow of electric current through the external electrodes. Under compression a positive voltage is generated and under expansion, a negative voltage is generated (Fig. S14b).

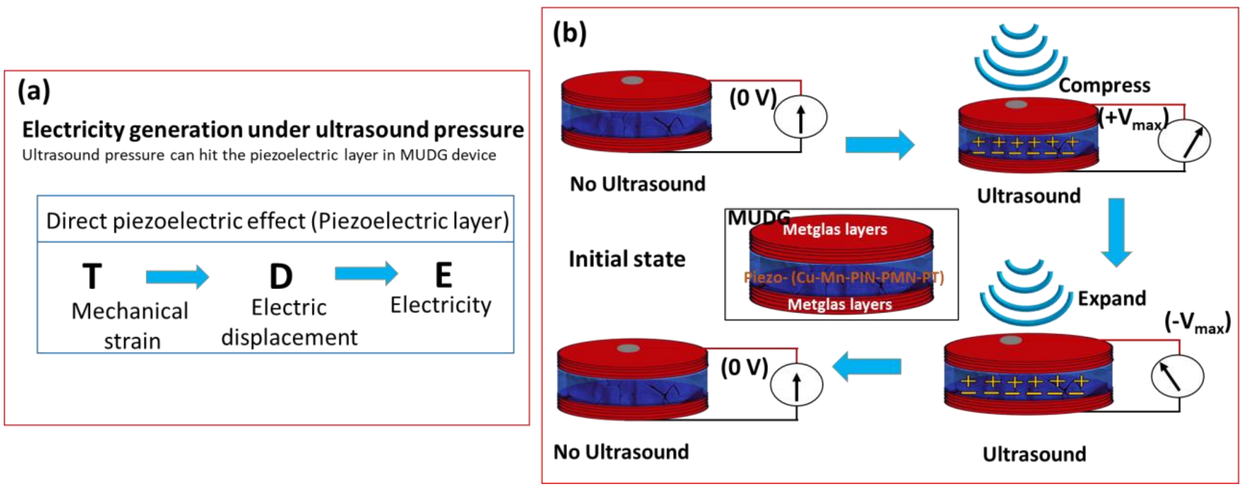

Fig. S14. (a) The transformation of ultrasound pressure to mechanical stress (T) in piezoelectric layer in ME device and generate electricity (E) via direct piezoelectric effect. (b) The working mechanism of electricity generation from MUDG device under ultrasound intense pressure. The 3D printed small parts.

Note S11. Measurement setup for dual energy harvesting

The measurement setup shown in Fig. S15 was used to harvest magnetic and ultrasound energy at the same time using single MUDG device. The MUDG devices were placed inside the water tank in such a way that the bottom part of the device is flat as shown in Fig. S15. To get the wires outside of the water tank we made two small holes in the container. To protect water leakage, the hot glue was used to seal the holes as shown in Fig. S10b.

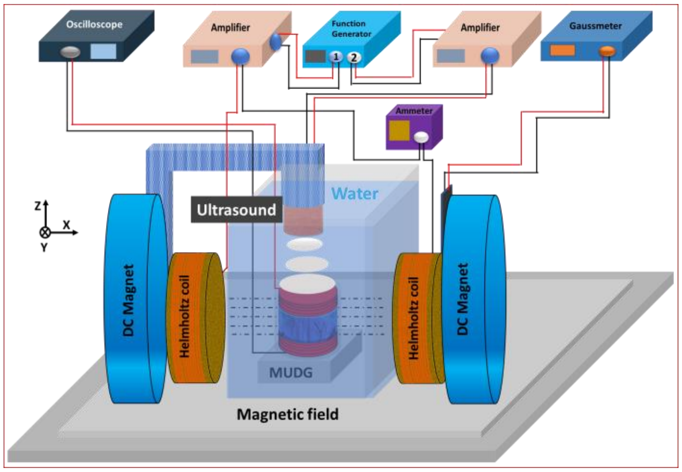

Fig. S15. Measurement setup for magnetic field and ultrasound based dual energy harvester.

Note S12. Relationship between input and output voltage of the dual energy harvester

The output voltage of MUDG devices increases linearly with the increasing input voltage for ultrasound at constant magnetic field (100 μT) and 250 kHz frequency (Fig. S16a).

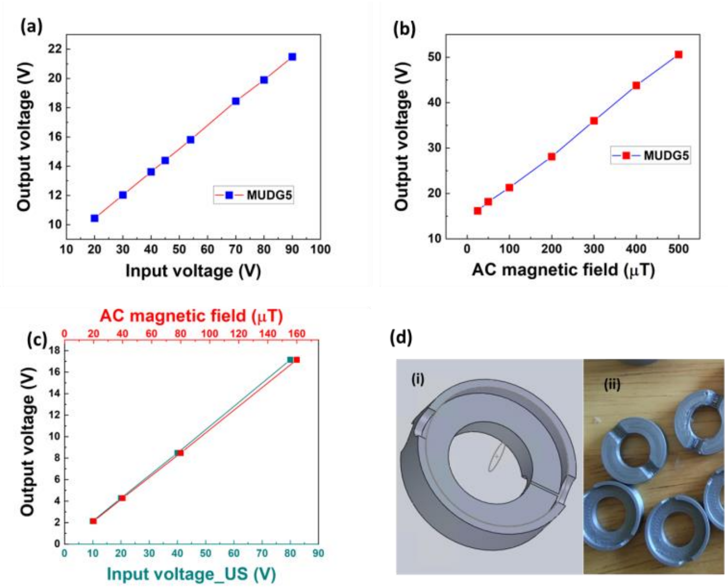

Fig. S16. (a) The relationship between the input voltage (Vp-p) and output voltage (Vp-p) of MUDG5 at constant AC magnetic field (100μT) during ultrasound measurement. (b) The relationship between the AC magnetic field and output voltage (Vp-p) of MUDG5 at constant input voltage (90Vp-p) applied to the ultrasound transducer. (c) The behaviour of output voltage (Vp-p) by changing AC magnetic field and input voltage (applied to the ultrasound transducer) simultaneously at constant frequency. (d) The 3D printed design (i) and real image (ii) of the holder used to avoid any misalignment of the device under tissue measurement.

Similarly at constant input voltage (90Vp-p applied to US transducer), with the increase of AC magnetic field the output voltage increases linearly at constant frequency of 250kHz (Fig. S16b). The generated voltage from the MUDG5 device also has linear relationship with the simultaneously change of AC magnetic field and input voltage applied to the ultrasound transducer at constant frequency (Fig. S16c). We used 3D printed holder for the MUDG device to avoid any misalignment during the measurement as shown in Fig. S16d(i,ii).

Note S13. Measurement of acoustic intensity using calibrated hydrophone

To verify the safety limit of generated power by commercial ultrasound transducer used as a transmitter in our measurements, we immersed it in a water tank located in front of a hydrophone at 5 mm distance, which generated the maximum peak pressure in all measurements (Fig. S17). Ultrasound acoustic intensity measurement for different operation frequency and different input power has been done using the calibrated HGL0085 hydrophone (Onda Corp., Sunnyvale, CA) connected to a digital oscilloscope (with 50 Ω termination) via the Onda AG-2010 preamplifier providing around 20 dB voltage gain.

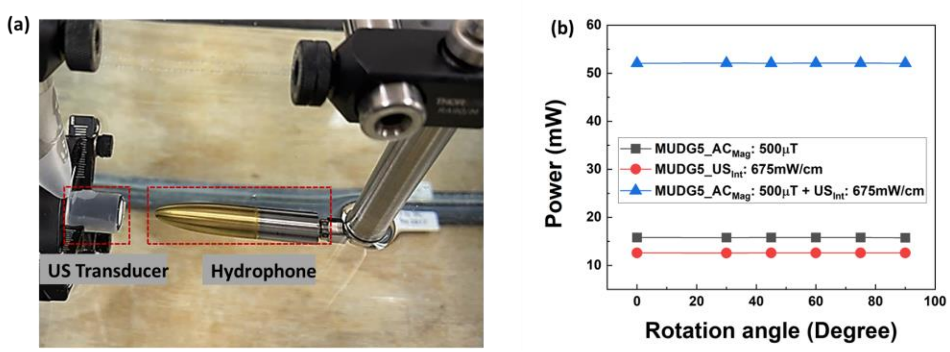

Fig. S17. (a) Measurement setup for the measurement of acoustic intensity of commercial transducer used in the present study. (b) The impact of power output when rotating the MUDG5 device along the z-axis (in xy plane).

To calculate output acoustic intensity characteristics in continuous mode the following equation has been used:[14]

$$I = \frac{V_{pp}^2}{8 \times M(f)^2 \times Z}$$

where V_{pp} is the receive peak-to-peak voltage across the hydrophone, $M(f)$ is the hydrophone's sensitivity (V/Pa) for a given frequency based on calibrated data sheet and Z is the acoustic impedance of the medium (Mrayl) which is the density of the medium multiplied by the sound speed in the medium indicating the level of resistance experienced by the propagating wave. For example, the measured acoustic intensity of the piezoelectric transducer for a frequency of 250 kHz, and the continuous input voltage of 160 V equivalent to 1.01 W/ cm^2 with hydrophone sensitivity of $4.299e^{-8}$ (V/Pa) and medium impedance of 1.482 Mrayl is ~484.0 mW/cm^2 which is below FDA time averaged acoustic intensity safety limit of ~675 mW/ cm^2 for body.[15]

Table S4: Calculated acoustic intensity of MUDG5 device depending on different input voltage applied to the ultrasound transducer at same frequency.

Frequency (kHz)	Input voltage is applied to the transducer (Vp-p)	Ultrasound input electrical power (W/cm^2)	Measured acoustic intensity (mW/cm^2)
250	45	~0.08	~40
250	90	~0.28	~137
250	114	~0.50	~243
250	160	~1.01	~484
250	192	~1.39	~675

Table S5. Comparison of the output performance of the MUDG device with that previously reported magnetoelectric, triboelectric, piezoelectric, ultrasound and dual energy harvesting devices.

Harvesting technique	**Active materials**	**Frequency**	**Input source**	**Power/Power density**	**Ref.**
Dual energy harvester	Metglas/ Cu-Mn-PIN-PMN-PT (Single device for magnetoelectric and ultrasound)	250kHz	Magnetic field (500µT RMS*), and Ultrasound energy (input power: 1W/cm^2 and Acoustic intensity: 570 mW/cm^2)	RMS Power (~52 mW) and power density (~597mW/cm^3 considering whole dimension	Present work (MUDG5)
	PFA/Au (Triboelectric) and PZT/Nickel (Magnetoelectric) (Two different circuits for output)	60Hz/143.2 Hz	Magnetic field (700µT RMS*) and mechanical energy	335.4 mW/cm^3	16
	Solar and Triboelectric energy harvester (Single device)	-----	Solar (80 mW/cm^2) and Mechanical	0.04 mW/cm^2	17
	Water/TiO_2 and PTFE/SiO_2 (Two different circuit for output)	-----	Trioelectric1 and Triboelectric2	0.131 and 0.038 mW/cm^2 (Peak power)	18

	F-KNN/Au/GNP	3.3 MHz and 1.0 MHz	Ultrasound and photoacoustic	278.8 and 10.2 mW cm^2 (Peak power)	19
Magnetoelectric energy harvester	Metglas/ Cu-Mn-PIN-PMN-PT	250 kHz	Magnetic field (500 µT RMS*)	RMS power ~16 mW and power density ~186 mW/cm^3	Present work (MUDG5)
	Metglas/PZT	250 kHz	Magnetic field (770 µT Peak*)	~2.16 mW (1.81 mW instantaneous peak power density at 500 µT RMS magnetic field) **	20
	Metglas/PZT	350 kHz	Magnetic field (>1000 µT Peak*)	~1.17 mW (0.58 mW power or 247 mW/cm^3 instantaneous peak power density at 500 µT RMS magnetic field) **	21
	Metglas/PZT5A	60 Hz	Magnetic field	~2.1 mW/cm^3	22
	Textured Fe–Ga/SCMF PMN–PZ–PT	60Hz	Magnetic field	3.22 mW/cm^3	23
Ultrasound energy harvester	Metglas/ Cu-Mn-PIN-PMN-PT	250kHz	Ultrasound intensity-675 mW/cm^2)	~145 mW/cm^3	Present work (MUDG5)

	Metglas/ Cu-Mn-PIN-PMN-PT	248 kHz	Ultrasound intensity ~675 mW/cm^2	~283 mW/cm^3	Present work (MUDG3)
	Lead zirconate titanate (PZT) diaphragm	240-250 kHz	Ultrasound intensity 1 mW/cm^2	3.75 $\mu W/cm^2$	24
	$[(K_{0.48}Na_{0.52})(Nb_{0.95}Sb_{0.05})$-$O_3$-$(Bi_{0.4}La_{0.1})(Na_{0.4}Li_{0.1})ZrO_3$	304 kHz	Ultrasound intensity ~5.887 W/cm2	45 mW/cm^2 (Estimated volume power density is 91.83 mW/cm^3 at ~720 mW/cm^2 ultrasound intensity) (Device thickness ~0.06 cm) (***)	25
	Perfluoroalkoxy (PFA) and Gold as triboelectric layers	20 kHz	Ultrasound input power 3 W/cm^2	~12.9 mW/cm^3 (***)	10
	Sm-doped $Pb(Mg_{1/3}Nb_{2/3})O_3$-$PbTiO_3$ (Sm-PMN-PT)	1MHz	Ultrasound intensity (20.3W/cm^2)	1.1 W/cm^2 (Estimated instantaneous volume power density is 195 mW/cm^3 (at ~720 mW/cm^2 ultrasound intensity) (Device thickness ~0.21 cm) (***)	26

	PZT 1-3	350 kHz	Ultrasound intensity ~65 mW/cm^2	1.41 μW/cm^2 (Estimated volume power density is ~1.26 mW/cm^3 (at ~720 mW/cm^2 ultrasound intensity) (Thickness 0.036 cm) (****)	27
Triboelectric energy harvester	Kapton/polyester	-----	Mechanical energy	10.4 mW/cm^3	28
	Cu/FEP/Au/Acrylic	3 kHz	Mechanical energy	19 mW/cm^2 (Peak)	29
	PVDF-TrFE @MoS_2/Nylon-11@MoS_2	6.5 Hz	Mechanical energy	~50 mW/cm^2 (Peak)	30
Piezoelectric energy harvester	PMN–PZT single crystals	2 Hz	Mechanical energy	0.26 mW	31
	ZnO nanowire textured film	----	Mechanical energy	10 mW/cm3 (Peak to Peak)	32
	PMN-PT single crystal MEMS	406.0 Hz	Vibration (14.7 m/s^2) energy	17.181mW/cm^3	33
	PZT MEMS	514.1 Hz	Vibration (9.8 m/s^2) energy	28.85 mW cm^3 (Peak Power)	34

	PZT	30 Hz	Vibration (6.9 m/s^2) energy	28.5 mW/cm^3	[35]

*****Magnetic peak input power is different from magnetic rms input power

** Estimated based on the data at similar applied magnetic field

*** Estimated based on the published data [26] at similar ultrasound intensity. Considered linear relationship between input ultrasound intensity and output power of the device at constant frequency.

**** Applied electrical power to the ultrasound transducer to generate ultrasound intensity.

Note S14. Working mechanism of MUDG under simultaneous magnetic field and ultrasound

The working mechanism of the MUDG device can be explained by the direct magnetoelectric and piezoelectric effect in different steps under simultaneous magnetic field and ultrasound, respectively (Fig. S18a,b). In the initial stage, when there is neither a magnetic field nor ultrasound present, the MUDG device does not produce any electrical charge. Subsequently, when a magnetic field is introduced, the ME device experiences stress and generates electrical charge through the direct magnetoelectric effect, resulting in electricity generation. When ultrasound pressure is also simultaneously applied, due to inherent mechanical property of the MUDG device, a higher strain and thus a higher generated voltage is generated. The amount of strain is directly proportional to the applied ultrasound pressure and the amount of magnetostriction (that depends on the magnetic field strength), that results in addition of the produced voltages. As the piezoelectric layer compresses under the combined influence of the magnetic field and ultrasound pressure, electrons flow from one electrode to another through an external circuit, causing the ME device to produce a positive signal. Similarly, when the piezoelectric layer expands or decompresses, electrons flow in the opposite direction through the external circuit, generating a negative signal. In the absence of ultrasound and solely under the influence of a magnetic field, the ME device once again produces a low output voltage due to reduced stress in the piezoelectric layer. In the final step, the ME device cannot generate any output signal because there is no stress generated in the piezoelectric layer in the absence of ultrasound and a magnetic field.

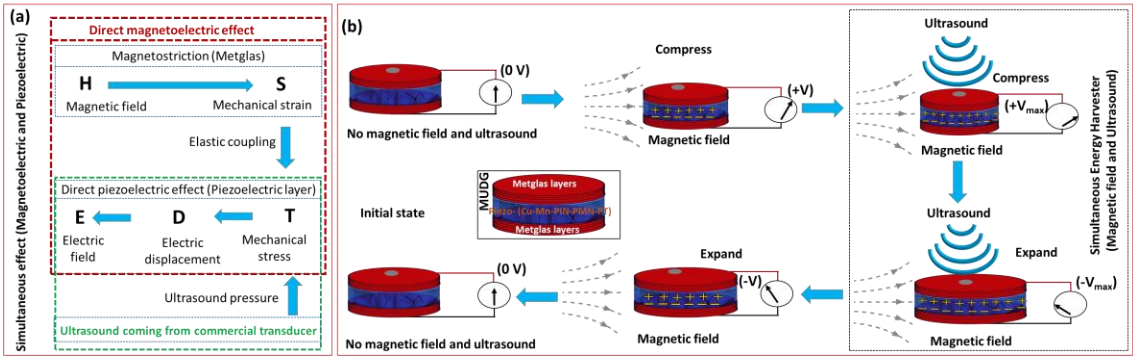

Fig. S18. (a) The principle of direct magnetoelectric and ultrasound pressure based direct piezoelectric effect. (b) Working mechanism of MUDG device under simultaneous magnetic field and ultrasound pressure.

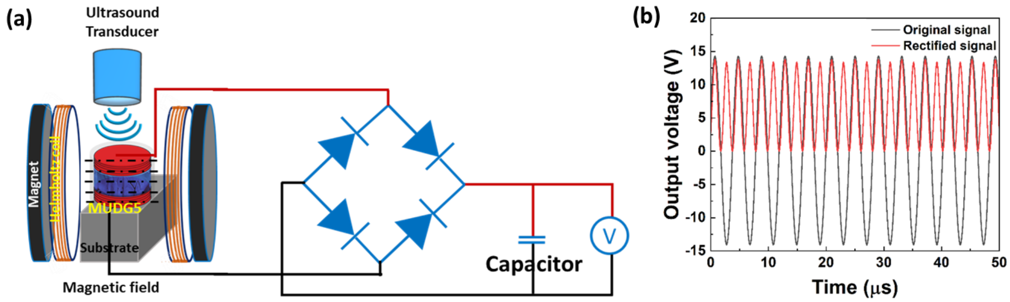

Fig. S19. (a) Measurement electrical circuit used to convert AC to DC signal using full bridge rectifier. (b) The measured AC and DC signal for MUDG5 during simultaneous measurement conditions (200 μT AC magnetic field and 137 mW/cm^{2}ultrasound intensity).

Table S6: The charging time, stored energy and storage power of the different capacitors was charged by MUDG5 device.

Capacitors	Applied energy	Charging time	Charging voltage	Energy stored	Storage Power
1 mF	100μT ME	1.0 min	5.6 V	15.68 mJ	0.26 mW
4.4 mF	100μT ME	4.0 min	5.5 V	66.55 mJ	0.277 mW
4.4 mF	0.2 W/cm^2 US	4.2 min	5.2 V	59.48 mJ	0.24 mW
10 mF	100μT ME	6.5 min	5.0 V	125.0 mJ	0.32 mW
10 mF	300μT ME	6.3 min	9.76 V	476.29 mJ	1.26 mW
Supercapacitor (1F)	300μT ME and 137 mW/cm^2 US	48.0 min	3.70 V	6845.0 J	2.37 W

Note S15. Electrical circuit for battery recharging

We have used Linear Technologies LTC3588-1 energy harvesting IC along with its application circuit as provided by the manufacturer in the data sheet. This IC was specifically chosen as it supported energy extraction with high efficiencies from high impedance piezoelectric devices. The capacitor that needed to be charged, was placed at $C_{STORAGE}$ in Fig. S20 and did not include the diode, the resistor, and the cell. To charge the different batteries with different capacities (1, 3, 5, 11 and 30 mAh), we used the circuit shown in Fig. S20. The charge limiting resistor in the circuit was used as per the cell manufacturer's recommendations (1, 3 amd 5 mAh batteries was charged with a current limiting resistor 2.2 kΩ). The 11 mAh battery (Seiko Industries) was charged using a current limiting resistor of 670 Ω and the 30 mAh battery (Panasonic) was charged with a current limiting resistor of 180 Ω.

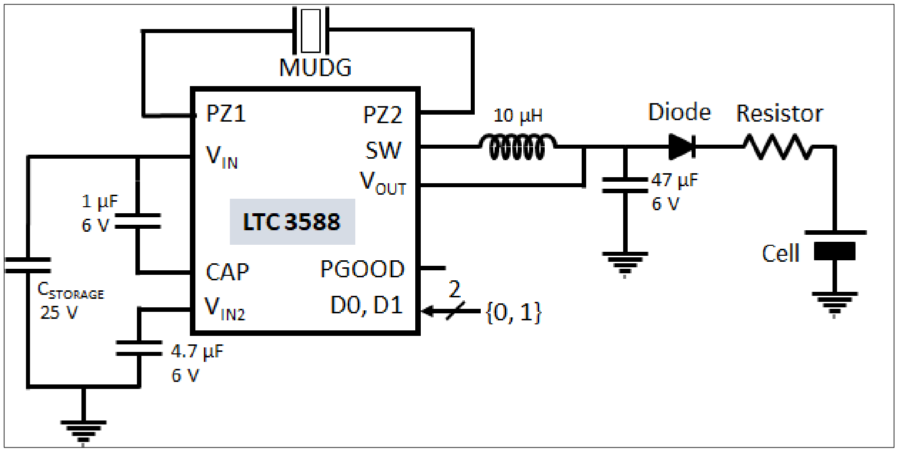

Fig. S20. Typical application LTC-3588 circuit used for energy harvesting and battery charging.

Note S16. Measurement setup for *ex-vivo* study

To measure the output power, the MUDG5 device was placed inside the porcine tissue and all the setup excluding electromagnet was placed under water (Fig. S21). The reason to put the coils inside the water was to release the weight of tissue that may be possible to restrict certain amount of vibration of the MUDG under weight. To check the performance of the MUDG5 device we did *ex-vivo* experiment under porcine tissue with the thickness of 5, and 15 mm.

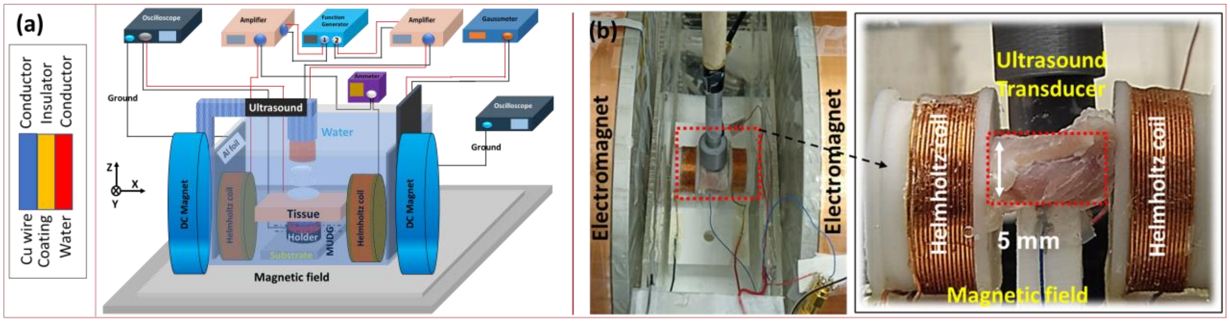

Fig. S21. (a) Measurement setup for the energy harvesting in presence of Porcine tissue with different thickness in water. (b) The real image of the measurement setup during battery charging under porcine tissue which is submerged in the water.

The Helmholtz coils were also submerged underwater to allow for more flexibility in the measurement. To measure the output power, the MUDG5 device was placed inside porcine tissue, and all components of the setup, except for the electromagnet, were also submerged underwater. This approach allowed for better control of any mismatch of the acoustic impedance between different media and enabled movement of the commercial transducer in different directions, such as axial or lateral. A diagram of the measurement setup is presented in Fig. S21. Capacitive coupling among the Cu wire coils, Parylene-C coating, and water was potentially eliminated by placing Al foils near the Helmholtz coils inside the water tank and connecting them to the ground of the oscilloscope. Although, the Parylene-C is a highly stable and reliable polymer to coat the implantable device for long time study without damage as stated by earlier study.[36] However, we have tested long durability measurement of MUDG5 device for 6 month through continuous measurement for 30min at each 1 month intervals (Fig. S22).

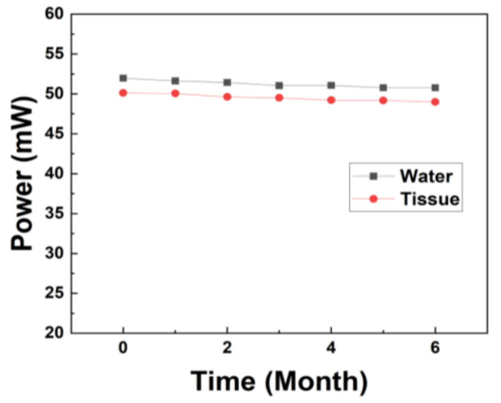

S22. The long-time durability test of the MUDG5 device operating continuously for 30 mins, tested at 1-month intervals.

Note 17. Oxygen plasma treatment and contact angles measurement

The surface's hydrophilic or hydrophobic characteristics play a pivotal role in influencing cell adhesion.[37] Typically, on hydrophilic surfaces, cells tend to spread extensively and forming robust focal adhesions. Conversely, on hydrophobic surfaces, the formation of focal adhesions is minimal, and cells maintain a rounded shape with reduced proliferation rates. [38] These observations align with prior research emphasizing the role of surface chemistry in promoting the adhesion of osteoblasts, where oxygen-containing groups such as -COOH and -OH are responsible for determining surface wettability.[36] In this study, we modified the surface of Parylene-C through oxygen plasma treatment for 1 and 5 minutes, aiming to enhance its hydrophilicity, as depicted in Fig. S23.

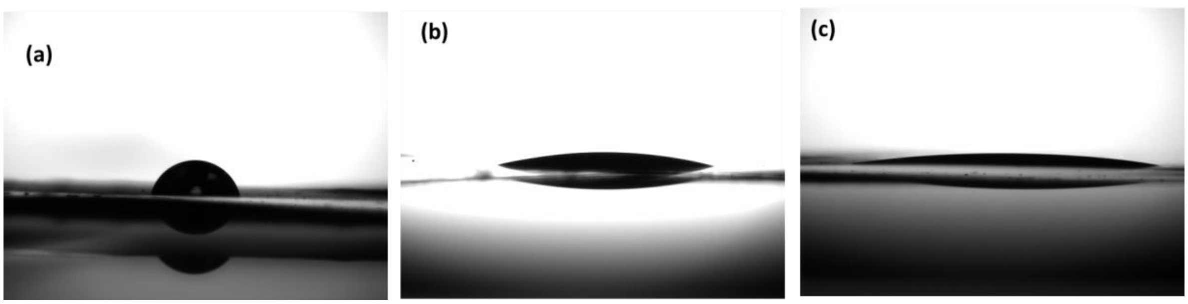

Fig. 23. Contact angle measurement of Parylene-C coated Metglas/MUDG device before (a) and after plasma coating for 1min (b) and 5 min (c)

The Parylene-C coated MUDG device exhibited a contact angle of 80°±1.2, indicating its initial hydrophobic nature. The alterations in surface morphology had a profound impact on Parylene-C's wettability. After 1-minute plasma treatment, the contact angle decreased to approximately 28°± 2 degrees, indicating a shift towards hydrophilicity. With a 5-minute treatment, the contact angle further reduced to around 19°±1.5, indicating enhanced functionalization and increased hydrophilicity. These results signify a transformation from a hydrophobic to a hydrophilic surface. This observation aligns with previous research, demonstrating that the formation of chemical functional groups like C=O, C–O, O–C=O, C–O–O, and O–C(O)–O during oxygen plasma treatment significantly boosts surface hydrophilicity.[39, 40]

Note 18. Cell adhesion test

In order to assess the biosafety and toxicity of Parylene-C, we conducted an encapsulation process on various samples, including coverslips, Metglas, and devices. Within MUDG devices, the magnetostrictive layers were positioned both above and below the piezoelectric layers, with Parylene-C serving as the outermost surface of these devices. Hence, we individually coated Metglas and coverslips with Parylene-C to facilitate easy validation. This precaution was taken because, following implantation, live cells may come into direct contact with the surface of Parylene-C. The assessment of cell adhesion on control cover slips, Parylene-C coated cover slips, and Parylene-C coated cover slips subjected to oxygen plasma treatment for 1 and 5 minutes can be gleaned from Fig. S24a-f. In Figure S24a-b, optical microscope images reveal that Huh7 cells exhibit robust adhesion to the control cover slips, while the Parylene-C coated sample display a comparatively lower number of adherent cells. However, in Fig. S24c, the oxygen plasma-treated sample for 1 minute displays a high level of cell adhesion with a uniform distribution, likely attributed to the favourable surface roughness and hydrophilic properties that are conducive to live cell adhesion, consistent with previous observations reported elsewhere.[36] However, in the case of Parylene-C coated samples treated with oxygen plasma for 5 minutes, a slight decrease in cells adherence is noted due to higher rough surface of Parylene-C as shown in Fig. S24d.

Similarly, the oxygen plasma treatment of Parylene-C coated Metglas surfaces shows uniform distribution of cells as evidenced in Figure S24e. Conversely, for Parylene-C coated Metglas treated with oxygen plasma for 5 minutes, there is a reduced number of adherent cells. These findings suggest that the creation of nano-irregularities along with the presence of oxygen-containing groups can promote cell growth on an oxygen plasma-treated Parylene-C surface.[36, 41] Therefore, oxygen plasma treatment may offers an alternative method for producing Parylene-C coated biomedical devices to promote good cell adhesion and limited cytotoxicity in the biomedical field. It is important to note that the introduction of oxygen through this process does not have a detrimental impact on cell growth and does not significantly affect biocompatibility.[40] While additional research is required to fully comprehend the influence of oxygen on surface properties, this is particularly critical in light of the interaction between drug molecules and the oxygen adsorption sites within the modified polymer coating.

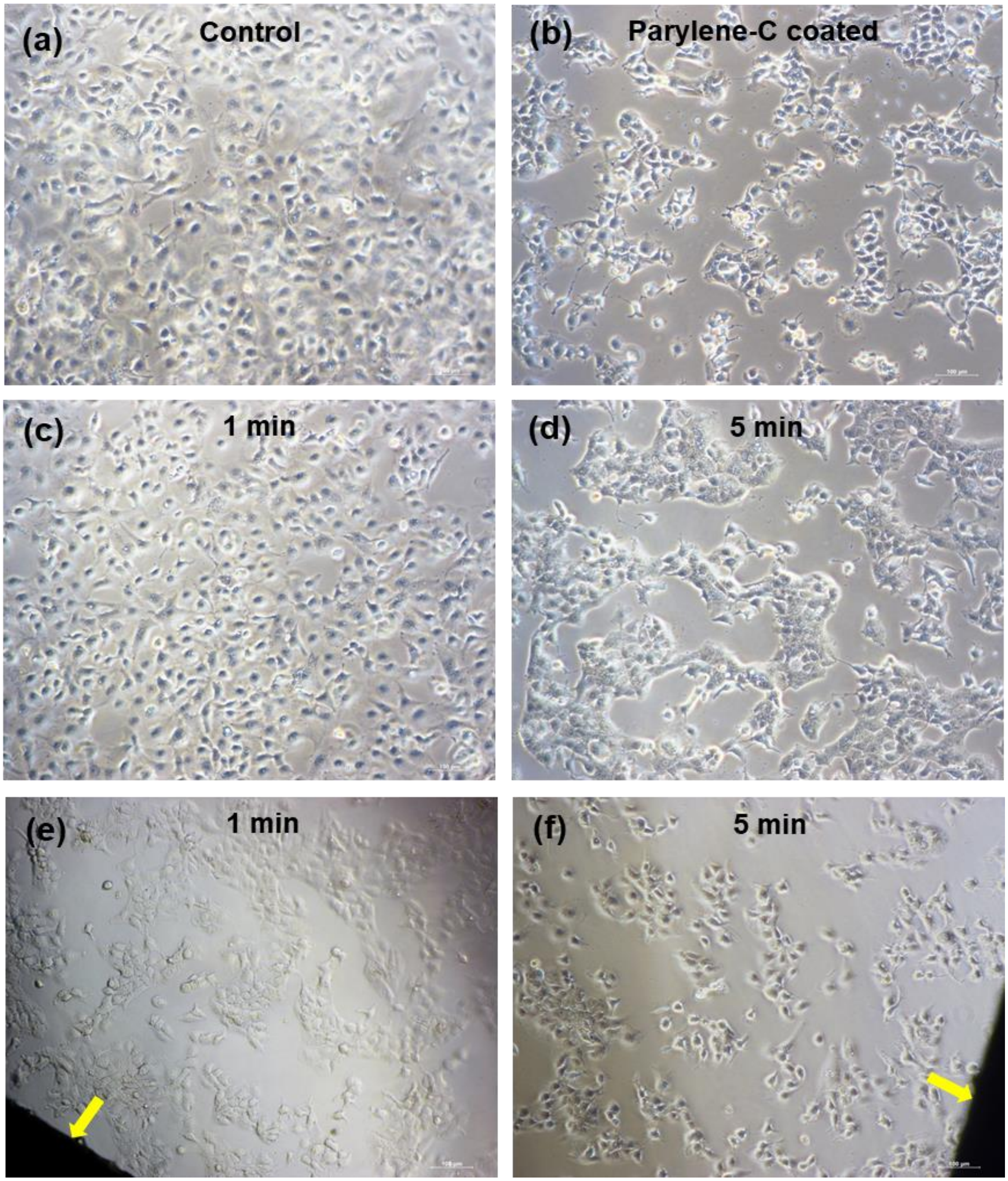

Fig. S24. Phase-contrast photomicrographs of Huh7 cells. Huh7 cells were cultured on Poly-L-Lysine coated coverslips. (a) control; (b) Parylene-C coated; (c,d) Parylene-C coated and treated with oxygen plasma for 1 min and 5 min; (e,f) cells grown in presence of foil coated with Parylene-C and treated with oxygen plasma for 1min and 5 min. Yellow arrows point to the Metglas. Scale bar: 100 μm.

References

1. D. Wang, M. Cao and S. Zhang, *Journal of the European Ceramic Society*, 2012, **32**, 433-439.
2. H. Leng, Y. Yan, H. Liu, M. Fanton, R. J. Meyer and S. Priya, *Acta Materialia*, 2021, **206**, 116610.
3. S. Zhang, F. Li, X. Jiang, J. Kim, J. Luo and X. Geng, *Progress in Materials Science*, 2015, **68**, 1-66.
4. S. Zhang and F. Li, *Journal of Applied Physics*, 2012, **111**, 2.
5. A. Kumar and A. Arockiarajan, *Smart Materials and Structures*, 2022, **31**, 083001.
6. D. K. Pradhan, S. Kumari and P. D. Rack, *Nanomaterials*, 2020, **10**, 2072.
7. L. Li, Y. Q. Lin and X. M. Chen, *Journal of Applied Physics*, 2007, **102**.
8. S. Hosur, R. Sriramdas, S. K. Karan, N. Liu, S. Priya and M. Kiani, *IEEE Transactions on Biomedical Circuits and Systems*, 2021, **15**, 1079-1092.
9. X. Zhuang, A. Nikoozadeh, M. Beasley, G. Yaralioglu, B. Khuri-Yakub and B. Pruitt, *Journal of Micromechanics and Microengineering*, 2007, **17**, 994.
10. R. Hinchet, H.-J. Yoon, H. Ryu, M.-K. Kim, E.-K. Choi, D.-S. Kim and S.-W. Kim, *Science*, 2019, **365**, 491-494.
11. D. Satkunskienė, V. Grigas, V. Eidukynas and A. Domeika, 2009, **11**, 506-510 .
12. K. Teknomo, *arXiv preprint arXiv:1610.00029*, 2016.
13. K. Kobayashi, S. Yoshida, Y. Saijo and N. Hozumi, *Ultrasonics*, 2014, **54**, 1922-1928.
14. S. Hosseini, K. Laursen, A. Rashidi, T. Mondal, B. Corbett and F. Moradi, *IEEE Transactions on Ultrasonics, Ferroelectrics, and Frequency Control*, 2020, **68**, 191-200.
15. Food and D. Administration, *Guidance for Industry and FDA Staff*, 2008.
16. K.-W. Lim, M. Peddigari, C. H. Park, H. Y. Lee, Y. Min, J.-W. Kim, C.-W. Ahn, J.-J. Choi, B.-D. Hahn and J.-H. Choi, *Energy & Environmental Science*, 2019, **12**, 666-674.
17. J. Chen, Y. Huang, N. Zhang, H. Zou, R. Liu, C. Tao, X. Fan and Z. L. Wang, *Nature Energy*, 2016, **1**, 1-8.
18. Z.-H. Lin, G. Cheng, W. Wu, K. C. Pradel and Z. L. Wang, *ACS nano*, 2014, **8**, 6440-6448.
19. L. Jiang, G. Lu, Y. Yang, Y. Zeng, Y. Sun, R. Li, M. S. Humayun, Y. Chen and Q. Zhou, *Energy & Environmental Science*, 2021, **14**, 1490-1505.

20. Z. Yu, J. C. Chen, F. T. Alrashdan, B. W. Avants, Y. He, A. Singer, J. T. Robinson and K. Yang, *IEEE Transactions on Biomedical Circuits and Systems*, 2020, **14**, 1241-1252.
21. J. C. Chen, P. Kan, Z. Yu, F. Alrashdan, R. Garcia, A. Singer, C. Lai, B. Avants, S. Crosby and Z. Li, *Nature Biomedical Engineering*, 2022, 1-11.
22. H. Lee, R. Sriramdas, P. Kumar, M. Sanghadasa, M. G. Kang and S. Priya, *Energy & Environmental Science*, 2020, **13**, 1462-1472.
23. V. Annapureddy, S.-M. Na, G.-T. Hwang, M. G. Kang, R. Sriramdas, H. Palneedi, W.-H. Yoon, B.-D. Hahn, J.-W. Kim and C.-W. Ahn, *Energy & Environmental Science*, 2018, **11**, 818-829.
24. Q. Shi, T. Wang and C. Lee, *Scientific Reports*, 2016, **6**, 1-10.
25. L. Jiang, Y. Yang, R. Chen, G. Lu, R. Li, J. Xing, K. K. Shung, M. S. Humayun, J. Zhu and Y. Chen, *Advanced Functional Materials*, 2019, **29**, 1902522.
26. T. Zhang, H. Liang, Z. Wang, C. Qiu, Y. B. Peng, X. Zhu, J. Li, X. Ge, J. Xu and X. Huang, *Science Advances*, 2022, **8**, eabk0159.
27. L. Jiang, Y. Yang, R. Chen, G. Lu, R. Li, D. Li, M. S. Humayun, K. K. Shung, J. Zhu and Y. Chen, *Nano Energy*, 2019, **56**, 216-224.
28. F.-R. Fan, Z.-Q. Tian and Z. L. Wang, *Nano Energy*, 2012, **1**, 328-334.
29. G. Zhu, J. Chen, T. Zhang, Q. Jing and Z. L. Wang, *Nature Communications*, 2014, **5**, 1-9.
30. M. Kim, D. Park, M. M. Alam, S. Lee, P. Park and J. Nah, *ACS Nano*, 2019, **13**, 4640-4646.
31. G. T. Hwang, J. Yang, S. H. Yang, H. Y. Lee, M. Lee, D. Y. Park, J. H. Han, S. J. Lee, C. K. Jeong and J. Kim, *Advanced Energy Materials*, 2015, **5**, 1500051.
32. Y. Hu, Y. Zhang, C. Xu, L. Lin, R. L. Snyder and Z. L. Wang, *Nano Letters*, 2011, **11**, 2572-2577.
33. G. Tang, B. Yang, J.-q. Liu, B. Xu, H.-y. Zhu and C.-s. Yang, *Sensors and Actuators A: Physical*, 2014, **205**, 150-155.
34. G. Tang, J.-q. Liu, B. Yang, J.-b. Luo, H.-s. Liu, Y.-g. Li, C.-s. Yang, D.-n. He, V. D. Dao and K. Tanaka, *Journal of Micromechanics and Microengineering*, 2012, **22**, 065017.
35. K.-H. Cho, H.-Y. Park, J. S. Heo and S. Priya, *Journal of Applied Physics*, 2014, **115**, 204108.

36. M. Golda-Cepa, K. Engvall, M. Hakkarainen and A. Kotarba, *Progress in Organic Coatings*, 2020, **140**, 105493.
37. M. Golda-Cepa, W. Kulig, L. Cwiklik and A. Kotarba, *ACS Applied Materials & Interfaces*, 2017, **9**, 16685-16693.
38. M. M. Gentleman and E. Gentleman, *International Materials Reviews*, 2014, **59**, 417-429.
39. T. Y. Chang, V. G. Yadav, S. De Leo, A. Mohedas, B. Rajalingam, C.-L. Chen, S. Selvarasah, M. R. Dokmeci and A. Khademhosseini, *Langmuir*, 2007, **23**, 11718-11725.
40. H. R. Holmes, E. L. Tan, K. G. Ong and R. M. Rajachar, *Biosensors*, 2012, **2**, 57-69.
41. S.-J. Kim, D.-S. Lee, I.-G. Kim, D.-W. Sohn, J.-Y. Park, B.-K. Choi and S.-W. Kim, *The Kaohsiung Journal of Medical Sciences*, 2012, **28**, 123-129.